Supplementary Information 1. Continuum and $C^{18}O$ emission maps

Figure 7 shows a comparison between continuum, $C^{18}O$ 3-2, and CS 7-6 emission from our ACA dataset, where the $C^{18}O$ 3-2 emission was integrated between ± 20 km s^{-1} from the source velocity. It is clear that the CS 7-6 emission is significantly offset from the central star, and is not a result of a pointing innacuracy. A residual map was created by subtracting the CS 7-6 integrated intensity map from the $C^{18}O$ 3-2 integrated intensity map. A 1σ clip was first applied to the CS data, and the $C^{18}O$ peak flux was then scaled to match that of the CS. The residuals were then divided by the rms of the CS data.

Supplementary Information 2. Abundance maps and contribution functions

Figure 8 shows CS and SO abundance maps, for both the C/O=0.5 region and C/O=1.5 wedge . Contribution functions for the CS 7-6 and SO 7_7-6_6+7_8-6_7 transitions are overlaid (25% and 75% contours).

Supplementary Information 3. Varying the size and position of the high-C/O wedge

Figure 9 shows the effect of varying the size and position of the high-C/O wedge on the modelled spectra. The wedge size is described by the arc subtended by the angle θ. The wedge position is described using the azimuthal angle ϕ (where ϕ = 0 points due west, and is measured positively anti-clockwise). A given angle ϕ corresponds to the position of the arc centre.

We vary the angular size of the high-C/O wedge between θ = 20° to 180°, while keeping the centre of the wedge arc fixed at ϕ = 0 (Figure 9, top panel). Asymmetries in the SO spectra are more pronounced for larger wedge angles, with increasing wedge sizes leading to decreasing peak fluxes on the red-shifted side of the spectrum. The CS spectrum remains highly asymmetric about the source velocity, regardless of wedge size, with larger wedges result in broader line profiles and higher peak fluxes.

We vary the angular position of the high-C/O wedge between ϕ = –60° to 60°, while keeping the angular size fixed at θ = 60° (Figure 9, bottom panel). Asymmetries in the SO spectra are most pronounced when the wedge points towards 60°, since this corresponds to the region of the disk in which line-of-sight velocities are most highly red-shifted. Rotating the arc position clockwise through to –60° results in a incrementally smaller contribution to the SO spectra from the highly red-shifted part of the disk, and therfore a more symmetric double-peaked structure. Similarly, the CS spectrum is most highly red-shifted when the high-C/O wedge is positioned at 60°, with a narrow profile and high peak flux. As the arc position is rotated clockwise through to –60°, the line becomes broader with smaller peak flux, with the peak of the line profile moving closer to the source velocity.

Supplementary Information 4. Temperature and density maps

Figure 10 shows the temperature and density maps for dust and gas in the HD 100546 disk model.

Supplementary Information 5. Cooling, freeze-out, and chemical timescales

We propose that material associated with a protoplanet in HD 100546's inner dust cavity casts a shadow on a region of the outer disk, resulting in the azimuthal chemical variations described in this work. In order for such material to cast a shadow covering an angular region of 60°, as prescribed by our model, the azimuthal extent of the material must be much larger than the host star. At a radial distance of 13 au, which is equivalent to the outer edge of the dust cavity, the necessary azimuthal extent of the shadowing material is $\sim$ 15 au. Additionally, the material must extend vertically such that the shadow enables freeze-out of H_2O in the upper layers of the disk atmosphere. Taking r = 100 au and z/r = 0.25 as a representative location for excess H_2O freeze-out (via comparison with the modelled H_2O snow surface, see Figure 5), the necessary vertical extent of the shadowing material is $\sim$ 3.2 au. This is reasonable, since hydrodynamic simulations of disks show that dust concentrations associated with large embedded protoplanets can be highly elongated, especially in the ϕ direction (e.g. Zhu et al., 2014).

If the material responsible for shadowing orbits at 13 au, it will complete one orbit in $\sim$ 30 years. A shadow covering an azimuthal region of 60° will therefore transit a given region of the disk in 30 $\times$ (60/360) = 5 years. This places an upper limit on the total time available for changes in the chemistry to occur such that the C/O ratio becomes super-solar. To assess the feasibility of this scenario, we present a simple analytical model that takes into consideration three important timescales; cooling, freeze-out, and chemical conversion.

The cooling timescale for a single dust grain is given by:

$$t_{\rm cooling} = \frac{mC\Delta T}{Q_{\rm rad}P} \tag{5}$$

where m is the mass of the dust grain, C is the specific heat capacity, ΔT is the change in temperature, and $P = A\sigma T^4$ is the radiative power of the dust grain (where A is the grain surface area, and σ is the Stefan-Boltzmann constant). $Q_{\rm rad}$ is the Planck mean efficiency for dust grains at temperatures between 10-250 K (where $Q_{\rm rad} = 1.25 \times 10^{-5} T_d^2 (r/1\mu m)$, where r is the grain radius).

We make the simplifying assumption that gas in the disk atmosphere is coupled to a population of small dust grains of equal size $r = 1\mu m$. Taking ρ = 4 g cm^{-3} as a typical value for grain density (based on silicate materials such as olivine), the grain mass is then $m = \rho(4/3\pi r^3) \approx 1.68 \times 10^{-14}$ kg. We take C = 2000 J kg^{-1} K^{-1}, which is again typical of silicate material. Finally, we make the simplification that all H_2O is in gaseous form at 200 K and in ice at 100 K i.e. ΔT = 100 K. For grains with radius $r = 1\mu m$ at 200 K, $Q_{\rm rad}$ = 0.5. The cooling timescale can then be calculated as:

$$t_{\rm cooling} = \frac{1.26 \times 10^{-14} \times 2000 \times (200 - 100)}{0.5 \times 4\pi(10^{-6})^2 \times 5.67 \times 10^{-8} \times 200^4} \approx 4.5 \text{ s} \tag{6}$$

We now consider the freeze-out timescale, which is dictated by the efficiency with which gas-phase H_2O molecules collide with cooled grains. The mean free path of a gas molecule is given by:

$$\mu = \frac{1}{n\pi r^2} \tag{7}$$

where n is the number density of the dust grains, and r is the grain radius. We extract values for n directly from our chemical model, from a range of grid cells that trace the location of the H_2O freeze-out in the upper disk atmosphere, then reduce the value by a factor of 100 to account for dust settling to the midplane.

The average gas speed of a molecule is given by:

$$v_{\rm rms} = \sqrt{\bar{v}^2} = \sqrt{\frac{3kT}{m}} \tag{8}$$

where k is the Boltzmann constant and m is the mass of the H_2O molecule. The freeze-out timescale, which is equal to the collision timescale, is then given by:

$$t_{\rm freeze} = \frac{\mu}{\nu_{\rm rms}} \quad (9)$$

We compute $t_{\rm freeze}$ for a range of gas-to-dust ratios between $\Delta_{\rm g/d}$ = 10 – 390, where the lower limit is taken from Kama et al. (2016) and the upper limit is based on constraints from modelling HD lines (see Section 3.3). We find that $t_{\rm freeze}$ can vary from $\sim$ 47 hours to 4500 years between r = 13 to 300 au, depending on $\Delta_{\rm g/d}$. These values are subject to large uncertainties because $n_{\rm dust}$ can vary quite dramatically depending on the precise location of the disk atmosphere from which it is extracted, in addition to uncertainties in $\Delta_{\rm g/d}$ due to dust settling and radial drift. While the simple calculations we present here relate to a single grain, these can reasonably be used as an approximation for the entire local grain population in the optically thin regime, which is a reasonable assumption for material in the upper surface layers of the disk.

Finally, we consider the relevant chemical timescales. We simulate the effects of shadowing by first extracting the final elemental and molecular abundances from our 'unshadowed' C/O=0.5 model, using these as an input for the shadow model. The total elemental gas-phase oxygen is then depleted by setting the input H_2O abundance to zero (representing total freeze-out). This complete removal of H_2O is not enough to increase the gas-phase C/O above unity, since the majority of element oxygen is tied up in atomic O and CO. However, our chemical models show that when H_2O is removed from the gas phase on such a large scale, the following chemical rebalance leads to a significant production of new gas-phase H_2O via the following pathway:

$$H_2 + O \rightarrow OH + H \quad (10)$$
$$H_2 + OH \rightarrow H_2O + H \quad (11)$$

The subsequent freeze-out of this newly-produced gas-phase H_2O therefore provides a route by with atomic oxygen can be removed from the gas phase, further elevating the C/O ratio. Additional oxygen (and carbon) may be removed by the conversion of gas-phase CO into CO_2 ice, via a surface reaction with OH radicals produced by UV irradiation of amorphous solid water:

$$CO + OH \rightarrow \textit{trans}-HOCO \quad (12)$$
$$\textit{trans}-HOCO \rightarrow \textit{cis}-HOCO \quad (13)$$
$$\textit{cis}-HOCO \rightarrow CO_2 + H \quad (14)$$

We can expect reactions 12 - 14 to be enhanced in the shadowed region, since the lower temperature locks a larger fraction of H_2O into ices. Laboratory experiments show that this pathway can permanently sequester gas-phase CO into CO_2 ice at temperatures between 40-60 K (well above the canonical CO freeze-out temperature), with an efficiency of up to 27% (van Scheltinga et al., 2022). While reactions 12 - 14 are not included in our chemical network, we take them into account by manually adjusting the abundances as follows. We adjust the initial conditions of our shadow model, depleting not only H_2O, but also a fraction of atomic O and CO, such that the resulting gas-phase C/O = 1.5 (see Section 3.3). We let the chemistry evolve and extract the CS and SO abundances as a function of time from key regions of the disk. We find that the newly elevated C/O ratio favours both the formation of CS and destruction of SO, primarily via the reactions:

$$C + SO \rightarrow CS + O \quad (15)$$
$$C + SO \rightarrow CO + S \quad (16)$$

These reactions have no activation barrier and so can proceed in cold gas. CS is formed at a faster rate than SO is destroyed, since there are prominent CS formation pathways in addition to reaction 15:

$$CH_2 + S \rightarrow CS + H_2 \quad (17)$$
$$C + HS \rightarrow CS + H \quad (18)$$

The effect of this time evolution on the CS and SO abundances and disk integrated line fluxes is illustrated in Figure 11. The CS 7-6 disk-integrated line flux steadily increases with time in the super-stellar C/O environment, with the SO 7_7-6_6 disk-integrated line flux showing the opposite trend. To approximate the timescale at which this phenomenon becomes apparent in observations, we define the chemical timescale as the period in which the CS abundance increases by a factor of two, and the SO abundance decreases by a factor of two, whichever is longest (see Figure 11). We calculate the chemical timescale at different radial regions in the disk, by extracting the variations in CS and SO abundance from key grid cells in the model (Figure 11, lower panels). We find that the chemical timescale varies between $\sim 2 \times 10^{-4}$ to $\sim$ 5 years, for radial regions between 13-300 au.

The combined results for cooling, freeze-out, and chemical conversion are illustrated in Figure 6. The total time is almost entirely dependent on the freeze-out timescale, since the cooling and chemical timescales are negligable compared to the shadow transit time. We show that, within the $\sim$ 5 year period it takes the shadow to transit a given region of the disk, the gas-phase C/O ratio can become super-solar within the inner $\sim$ 200 au of the disk (within $\sim$ 150 au for $\Delta_{\rm g/d}$ = 100). Considering the fact that prominent emission from both CS and SO emanates from inside of $\sim$ 200 au (Supplementary Information 2), and the uncertainties associated with the freeze-out timescale, we conclude that shadowing is a plausible means by which the local C/O ratio can become elevated, leading to the spatial and spectral asymmetries presented in this work.

A more sophisticated model could take into account the reverse timescale, and the cyclical nature of disk shadowing, by addressing the effects of many transits over the lifetime of the disk. Such an investigation is beyond the scope of this work.

Supplementary Information 6. CS 7-6 channel maps

Figure 12 shows the individual channel maps for the CS 7-6 detection with the ACA.

Supplementary Information 7. CO 6-5, CO 3-2, and [CI] spectra

Figure 13 shows the modelled and observed CO 6-5, CO 3-2, and [CI] 1-0 spectral lines, used to constrain the level of CO depletion in the high-C/O wedge (see Section 3.3).

Supplementary Information 8. Disk model parameters

The parameters used in our disk models are listed in Table 1.

Supplementary Information 9. Observational data

The observational parameters for each of the spectral windows in the ACA dataset are given in Table 2. The full list of line fluxes and upper limits used to constrain our model is given in Table 3.

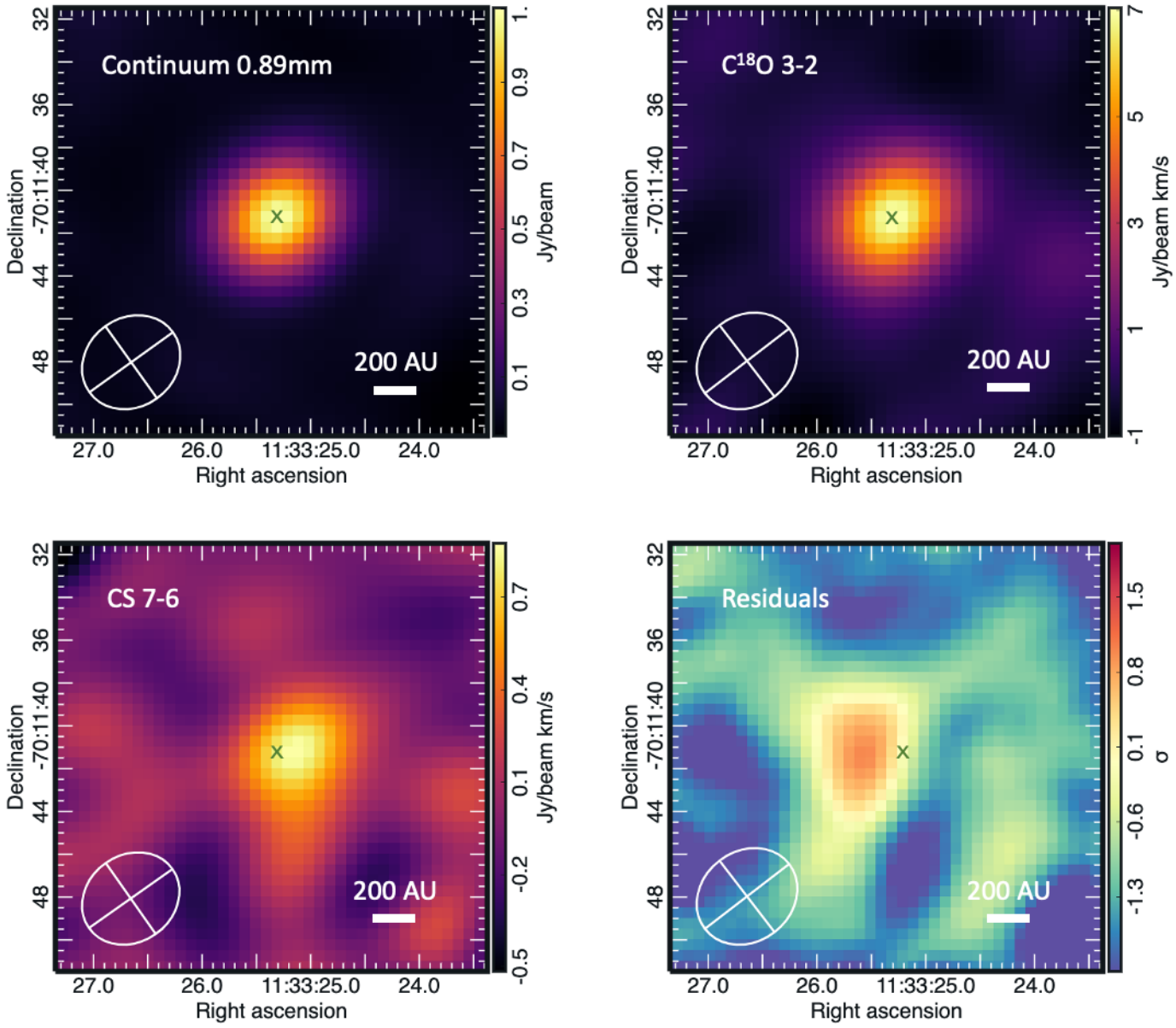

Figure 7. Comparison between continuum, $C^{18}O$, and CS ACA data, demonstrating pointing accuracy. *Top left:* Continuum emission map. *Top right:* $C^{18}O$ 3-2 integrated intensity map. *Bottom left:* CS 7-6 integrated intensity map. *Bottom right:* Residual map created by subtracting the CS emission from the $C^{18}O$ emission. The $C^{18}O$ flux was scaled to match the peak flux of the CS emission, and a 1σ clip was applied to the CS emission. The residuals are divided by the rms of the CS data, from which it is evident that the CS emission is significantly offset from the star (denoted with 'x').

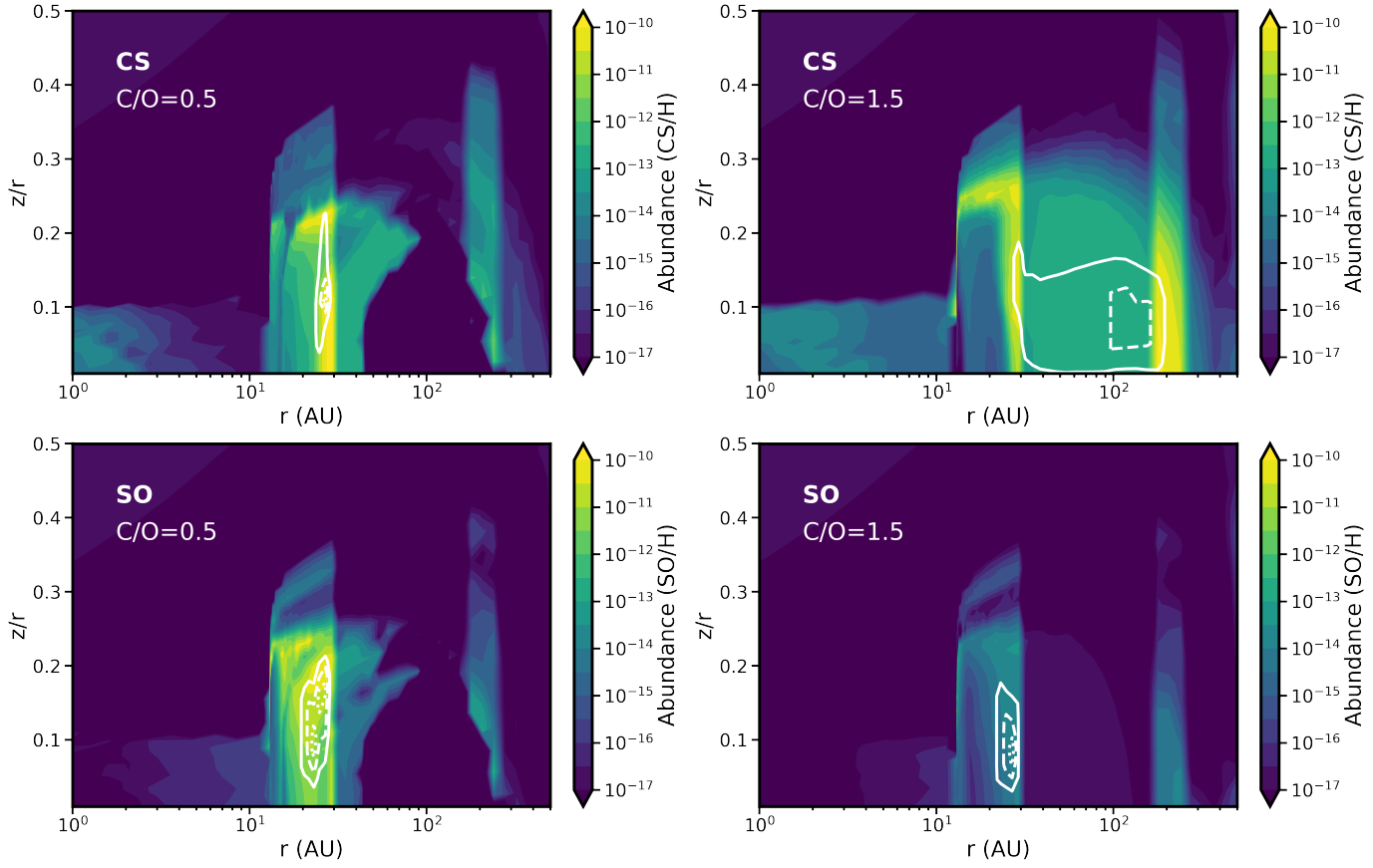

Figure 8. Abundance maps and contribution functions for the modelled CS and SO emission in HD 100546. Each panel shows an abundance map overlaid with contours representing 25% and 75% line emission (white). Top: CS 7-6 emission from the C/O=0.5 region (*left*) and C/O=1.5 wedge (*right*). Bottom: SO $7_7 - 6_6$+$7_8 - 6_7$ emission from the C/O=0.5 region (*left*) and C/O=1.5 wedge (*right*).

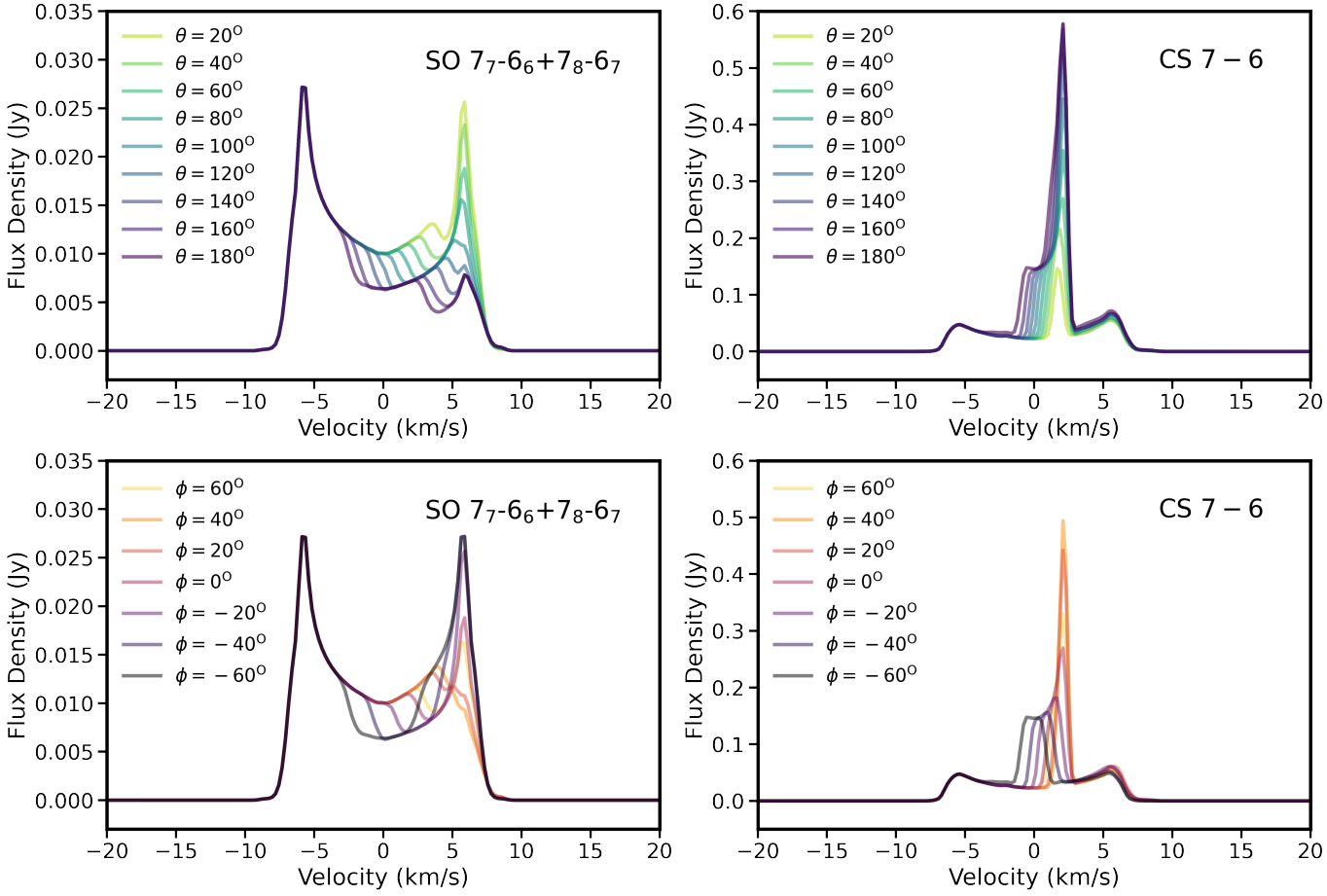

Figure 9. Effect of varying the high-C/O wedge size and position on the modelled spectra. *Top panel:* SO 7_7-6_6+7_8-6_7 (left) and CS $7-6$ (right) spectra for variations in wedge size (θ), centered on position $\phi = 0$. *Bottom panel:* SO 7_7-6_6+7_8-6_7 (left) and CS $7-6$ (right) spectra for variations in wedge position (ϕ), for a fixed angular size $\theta = 60^\circ$.

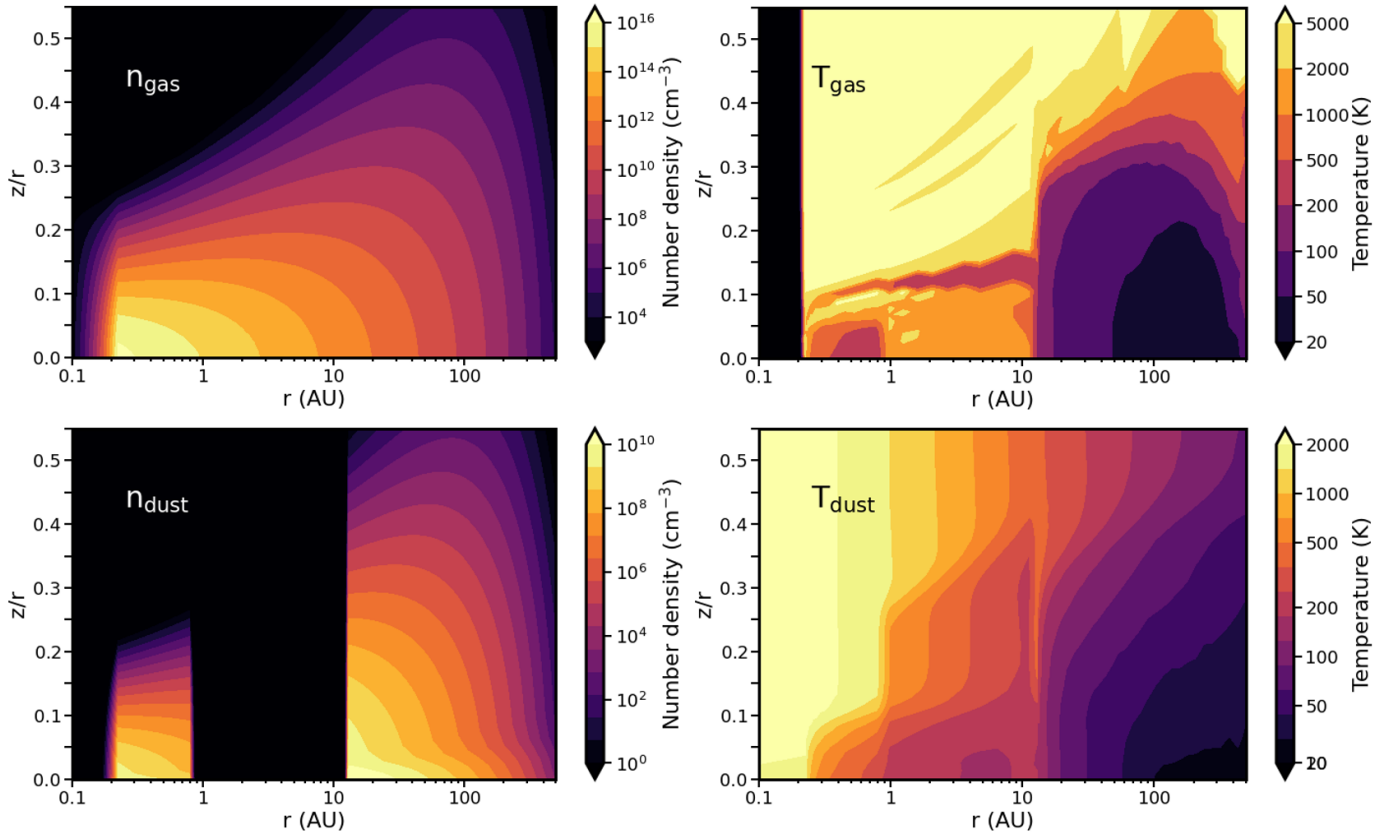

Figure 10. Temperature and density maps for the HD 100546 disk model. *Top left:* Gas number density. *Bottom left:* Dust number density. *Top right:* Gas temperature. *Bottom right:* Dust temperature.

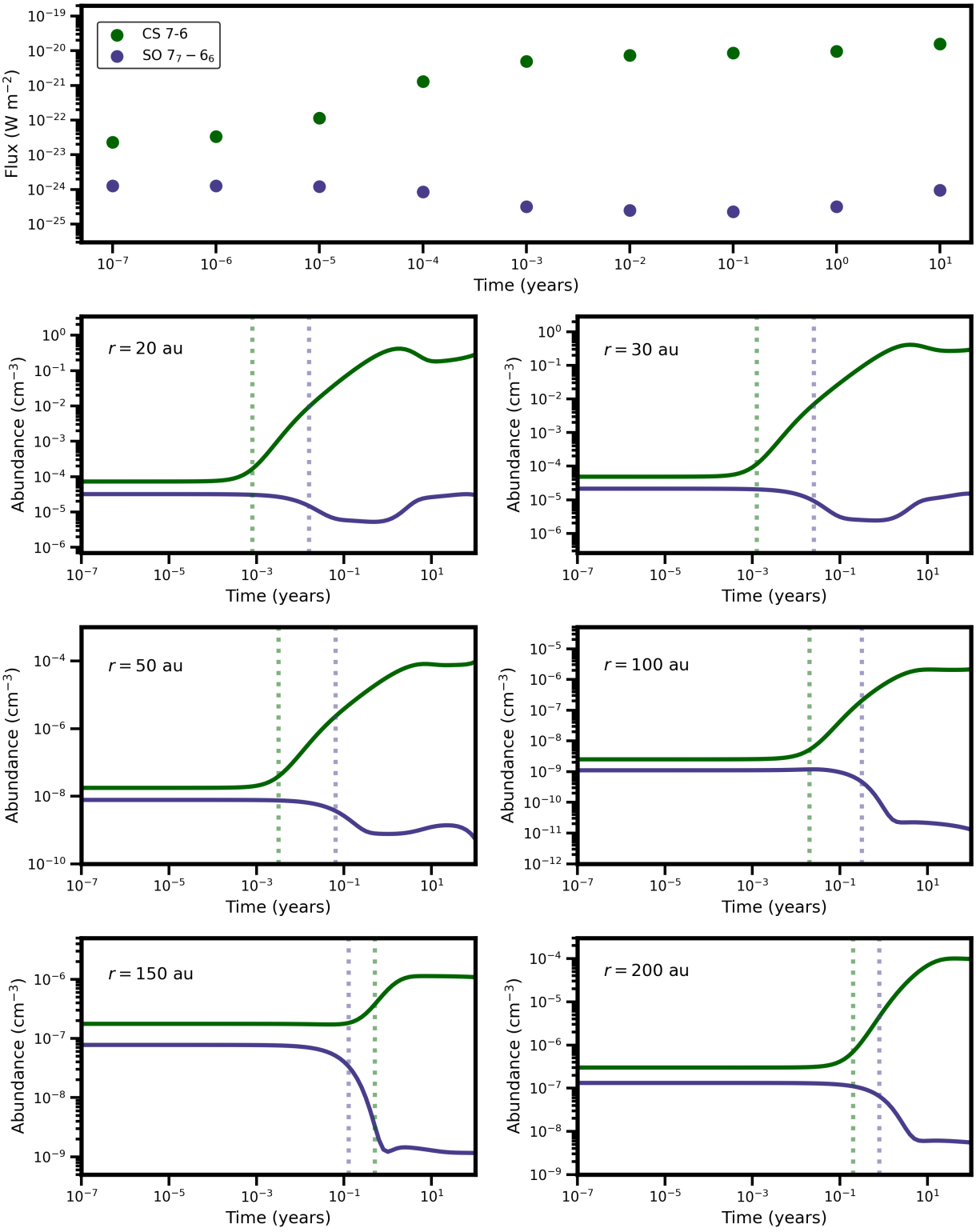

Figure 11. Time-dependent disk-integrated fluxes and abundances in the high C/O wedge. *Top panel:* Disk-integrated CS $7-6$ (green) and SO $7_7 - 6_6$ (blue) fluxes, as a function of time in the region where C/O=1.5. *All other panels:* CS (green) and SO (blue) abundances at different radial locations, as a function of time in the region where C/O=1.5. All values are extracted from the model at z/r ~ 0.25. Dotted lines represent the point in time where the CS flux increases by a factor of two from its initial values (green), and the SO flux decreases by a factor of two from its initial value (blue). The longer of these two times is taken as the chemical timescale at that particular radius.

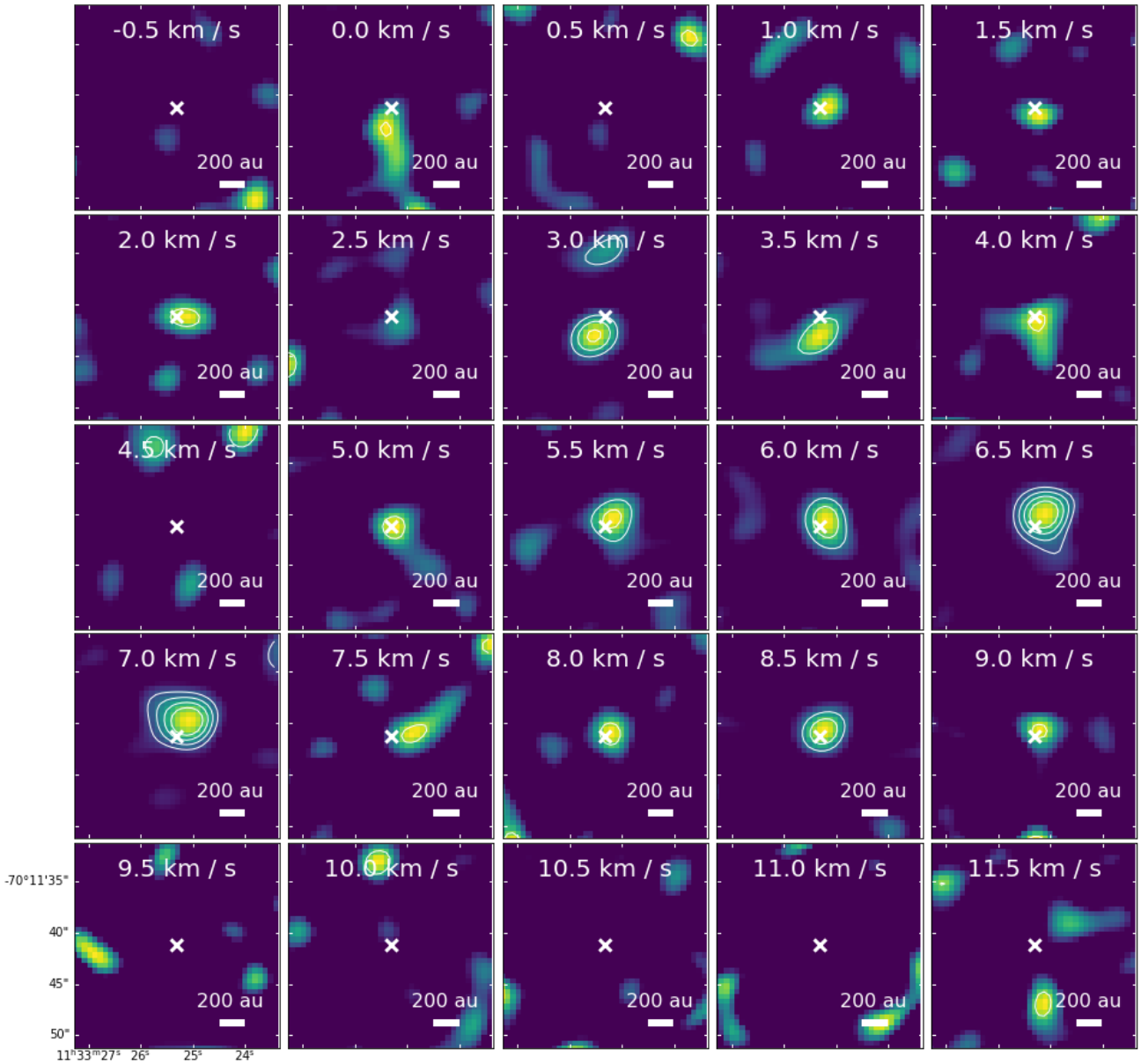

Figure 12. CS 7-6 channel maps at a spectral resolution of 0.5 km s^{-1}. Contours are at 35%, 50%, 65%, and 80% peak flux. The source velocity is $V_{\rm LSRK}$ = 5.7 km s^{-1}. The white cross denotes the position of the star.

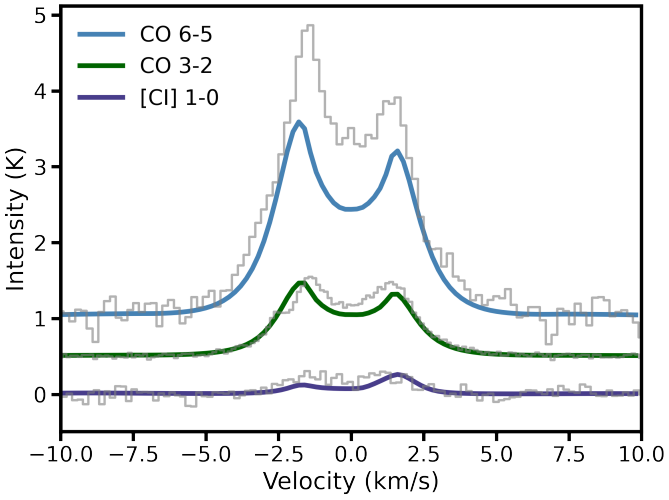

Figure 13. Modelled and observed CO and [CI] spectra. Modelled CO 6-5 (blue), CO 3-2 (green), and [CI] 1-0 (red) spectra. APEX observations in grey. The model reproduces the asymmetry of the CO 6-5 spectral line (but underpredicts the peak CO 6-5 flux, as in previous studies of HD 100546 (Kama et al., 2016)).

Table 1. HD 100546 disk model parameters.

Parameter	Description	Fiducial
$R_{\rm sub}$	Sublimation radius	0.25 au
$R_{\rm gap}$	Inner disk size	1.0 au
$R_{\rm cav}$	Cavity radius	13 au
$R_{\rm out}$	Disk outer radius	1000 au
R_c	Critical radius for surface density	50 au
$\delta_{\rm gas}$	Gas depletion factor inside cavity	1
$\delta_{\rm dust}$	Dust depletion factor inside cavity	10^{-4}
γ	Power law index of surface density profile	1.0
χ	Dust settling parameter	0.2
f	Large-to-small dust mixing parameter	0.85
Σ_c	$\Sigma_{\rm gas}$ at R_c	82.75 g cm^{-2}
h_c	Scale height at R_c	0.10
ψ	Power law index of scale height	0.20
$\Delta_{\rm g/d}$	Gas-to-dust mass ratio	100
L_*	Stellar luminosity	$36\ L_\odot$
L_X	Stellar X-ray luminosity	7.94×10^{28} erg s^{-1}
T_X	X-ray plasma temperature	7.0×10^7 K
$\zeta_{\rm cr}$	Cosmic ray ionization rate	3.0×10^{-17} s^{-1}
$M_{\rm gas}$	Disk gas mass	$1.45 \times 10^{-1}\ M_\odot$
$M_{\rm dust}$	Disk dust mass	$1.12 \times 10^{-3}\ M_\odot$
$[{\rm C/H}]_{\rm gas}$	Initial carbon abundance (relative to hydrogen)	1.0×10^{-5} (where C/O=0.5)[a]
$[{\rm O/H}]_{\rm gas}$	Initial oxygen abundance (relative to hydrogen)	2.0×10^{-5} (where C/O=0.5)[a]
$t_{\rm chem}$	Timescale for time-dependent chemistry	5 Myr (where C/O=0.5)[a]

[a]See Section 3.3 and Supplementary Information 5 for details on the chemical inputs to the C/O=1.5 'wedge' model

Table 2. Observational parameters for molecular species in HD 100546 from the ACA (program 2016.1.01339.S). Upper limits are at 3σ level, denoted by '<'.

Molecule	Transition	ν (GHz)[a]	Δ_ν (GHz)	$E_{\rm up}$ (K)[a]	$A_{\rm ul}$ (s^{-1})[a]	Beam Size	RMS (Jy beam^{-1} km s^{-1})	Flux (Jy km s^{-1})
SO	2_1-1_0	329.385	0.250	15.8	1.423×10^{-5}	4.83" × 4.08"	0.14	< 0.66
SO_2	$4_{3,1}$-$3_{2,2}$	332.505	0.250	31.3	3.290×10^{-4}	4.84" × 4.07"	0.10	< 0.48
$C^{36}S$	7 – 6	332.510	0.250	63.9	6.951×10^{-4}	4.78" × 4.07"	0.10	< 0.46
HCS^+	8 – 7	341.339	0.250	73.7	8.352×10^{-4}	4.62" × 4.03"	0.14	< 0.71
CS	7 – 6	342.883	0.250	65.8	8.368×10^{-4}	4.96" × 4.23"	0.10	0.62[b], 1.02[c]
H_2CS	$10_{0,10}$-$9_{0,9}$	342.946	0.250	90.6	6.080×10^{-4}	4.73" × 3.90"	0.31	< 1.50
^{34}SO	2_3-2_1	343.851	0.250	20.9	1.382×10^{-7}	4.63" × 3.89"	0.31	< 1.60
SO	8_8-7_7	344.310	0.250	87.5	5.188×10^{-4}	4.62" × 3.89"	0.30	< 1.50
$C^{18}O$	3 – 2	329.330	0.250	31.6	2.172×10^{-6}	4.96" × 4.21"	0.30	5.41[b], 8.22[c]

[a]Line frequencies, upper energy levels ($E_{\rm up}$), and Einstein A coefficients ($A_{\rm ul}$) are taken from the Cologne Database for Molecular Spectroscopy (CDMS; Müller et al., 2001; Müller et al., 2005; Endres et al., 2016) and the Leiden Atomic and Molecular Database (LAMDA; Schöier et al., 2005)

[b]Keplerian masked cube

[c]Elliptically masked cube

Table 3. Disk-integrated line fluxes and upper limits used to constrain our model

Molecule	Transition	Flux (W m^{-2})	Reference
CO	3-2	$1.72 \pm 0.04 \times 10^{-18}$	Kama et al. (2016)
CO	6-5	$1.61 \pm 0.08 \times 10^{-17}$	Kama et al. (2016)
CO	7-6	$2.35 \pm 0.27 \times 10^{-17}$	van der Wiel et al. (2014)
CO	8-7	$3.31 \pm 0.35 \times 10^{-17}$	van der Wiel et al. (2014)
CO	9-8	$4.53 \pm 0.41 \times 10^{-17}$	van der Wiel et al. (2014)
CO	10-9	$5.53 \pm 0.37 \times 10^{-17}$	van der Wiel et al. (2014)
CO	11-10	$5.13 \pm 0.45 \times 10^{-17}$	van der Wiel et al. (2014)
CO	12-11	$5.83 \pm 0.33 \times 10^{-17}$	van der Wiel et al. (2014)
CO	13-12	$6.07 \pm 0.47 \times 10^{-17}$	van der Wiel et al. (2014)
CO	14-13	$6.00 \pm 0.83 \times 10^{-17}$	Meeus et al. (2012)
CO	15-14	$8.83 \pm 0.97 \times 10^{-17}$	Meeus et al. (2012)
CO	16-15	$5.88 \pm 0.97 \times 10^{-17}$	Meeus et al. (2012)
CO	17-16	$7.39 \pm 1.0 \times 10^{-17}$	Meeus et al. (2012)
CO	18-17	$7.15 \pm 0.69 \times 10^{-17}$	Meeus et al. (2012)
CO	19-18	$6.47 \pm 0.85 \times 10^{-17}$	Meeus et al. (2012)
CO	20-19	$4.99 \pm 0.57 \times 10^{-17}$	Meeus et al. (2012)
CO	21-20	$6.50 \pm 0.88 \times 10^{-17}$	Meeus et al. (2012)
CO	22-21	$\leq 4.2 \times 10^{-17}$	Meeus et al. (2012)
CO	23-22	$7.84 \pm 1.1 \times 10^{-17}$	Meeus et al. (2012)
CO	24-23	$7.13 \pm 1.2 \times 10^{-17}$	Meeus et al. (2012)
CO	25-24	$\leq 7.71 \times 10^{-17}$	Meeus et al. (2012)
CO	28-27	$8.15 \pm 1.1 \times 10^{-17}$	Meeus et al. (2012)
CO	29-28	$7.86 \pm 1.9 \times 10^{-17}$	Meeus et al. (2012)
CO	30-29	$7.34 \pm 1.5 \times 10^{-17}$	Meeus et al. (2012)
CO	31-30	$\leq 1.40 \times 10^{-16}$	Meeus et al. (2012)
CO	32-31	$\leq 6.53 \times 10^{-17}$	Meeus et al. (2012)
CO	33-32	$\leq 8.45 \times 10^{-17}$	Meeus et al. (2012)
CO	34-33	$5.31 \pm 1.4 \times 10^{-17}$	Meeus et al. (2012)
CO	35-34	$\leq 4.41 \times 10^{-17}$	Meeus et al. (2012)
CO	36-35	$5.29 \pm 1.3 \times 10^{-17}$	Meeus et al. (2012)
CO	37-36	$\leq 8.29 \times 10^{-17}$	Meeus et al. (2012)
CO	38-37	$\leq 1.07 \times 10^{-16}$	Meeus et al. (2012)
^{13}CO	3-2	$\leq 6.6 \times 10^{-19}$	Panic et al. (2010)
^{13}CO	6-5	$\leq 7.5 \times 10^{-18}$	van der Wiel et al. (2014)
^{13}CO	7-6	$\leq 7.2 \times 10^{-18}$	van der Wiel et al. (2014)
^{13}CO	8-7	$\leq 1.02 \times 10^{-17}$	van der Wiel et al. (2014)
^{13}CO	9-8	$\leq 1.44 \times 10^{-17}$	van der Wiel et al. (2014)
^{13}CO	11-10	$\leq 1.68 \times 10^{-17}$	van der Wiel et al. (2014)
OI	145μm	$3.57 \pm 0.13 \times 10^{-16}$	Meeus et al. (2012), Fedele, D. et al. (2013)
OI	63μm	$5.54 \pm 0.05 \times 10^{-15}$	Meeus et al. (2012), Fedele, D. et al. (2013)
CI	1-0	$6.60 \pm 2.0 \times 10^{-19}$	Kama et al. (2016)
CI	2-1	$\leq 3.58 \times 10^{-18}$	Kama et al. (2016)
CII	158μm	$1.35 \pm 0.15 \times 10^{-16}$	Meeus et al. (2012), Fedele, D. et al. (2013)
HD	112μm	$\leq 2.7 \times 10^{-16}$	Kama et al. (2016)
HD	56μm	$\leq 1.6 \times 10^{-17}$	Fedele, D. et al. (2013)
C_2H	29	$\leq 4.8 \times 10^{-21}$	Kama et al. (2016)
C_2H	30	$\leq 4.8 \times 10^{-21}$	Kama et al. (2016)
C_2H	31	$\leq 4.8 \times 10^{-21}$	Kama et al. (2016)
C_2H	32	$\leq 4.8 \times 10^{-21}$	Kama et al. (2016)
C_2H	33	$\leq 4.8 \times 10^{-21}$	Kama et al. (2016)
C_2H	34	$\leq 4.8 \times 10^{-21}$	Kama et al. (2016)
C_2H	35	$\leq 4.8 \times 10^{-21}$	Kama et al. (2016)
C_2H	36	$\leq 4.8 \times 10^{-21}$	Kama et al. (2016)
C_2H	37	$\leq 4.8 \times 10^{-21}$	Kama et al. (2016)
C_2H	38	$\leq 4.8 \times 10^{-21}$	Kama et al. (2016)
C_2H	39	$\leq 4.8 \times 10^{-21}$	Kama et al. (2016)
HCO^+	1-0	$\leq 7.0 \times 10^{-20}$	Kama et al. (2016)
HCO^+	4-3	$6.81 \pm 1.0 \times 10^{-20}$	Kama et al. (2016)
H_2O	63.32	$\leq 2.59 \times 10^{-17}$	Meeus et al. (2012)
H_2O	71.946	$\leq 5.09 \times 10^{-17}$	Meeus et al. (2012)
H_2O	78.74	$\leq 5.70 \times 10^{-17}$	Meeus et al. (2012)
H_2O	179.52	$3.05 \pm 4.8 \times 10^{-17}$	Sturm et al. (2010)
H_2O	180.42	$\leq 1.71 \times 10^{-17}$	Meeus et al. (2012)
H_2O	90.00	$1.160 \pm 0.161 \times 10^{-16}$	Sturm et al. (2010)
H_2O	557 GHz	$1.41 \pm 0.0259 \times 10^{-18}$	Du et al. (2017)
H_2O	1113 GHz	$5.09 \pm 0.0844 \times 10^{-18}$	Du et al. (2017)
H_2O	1153 GHz	$\leq 1.98 \times 10^{-17}$	Du et al. (2017)

SO	7_7-6_6	1.25×10^{-21}	Booth et al. (accepted)
SO	7_8-6_7	1.45×10^{-21}	Booth et al. (accepted)
$C^{18}O$	3-2	9.03×10^{-20}	This work
SO	2_1-1_0	$< 7.25 \times 10^{-21}$	This work
SO_2	$4_{3,1}$-$3_{2,2}$	$< 5.32 \times 10^{-21}$	This work
$C^{36}S$	7-6	$< 5.10 \times 10^{-21}$	This work
HCS^+	8-7	$< 8.08 \times 10^{-21}$	This work
CS	7-6	1.167×10^{-20}	This work
H_2CS	$10_{0,10}$-$9_{0,9}$	$< 1.72 \times 10^{-20}$	This work
^{34}SO	2_3-2_1	$< 1.84 \times 10^{-20}$	This work
SO	8_8-7_7	$< 1.72 \times 10^{-20}$	This work